44th AIAA Aerospace Sciences Meeting and Exhibit
9 - 12 January 2006, Reno, Nevada

AIAA 2006-158

Numerical Simulation of Premixed Flame Quenching in the Broken-Reaction-Zone Regime

G. Eggenspieler*and S. Menon†
School of Aerospace Engineering
Georgia Institute of Technology
Atlanta, Georgia 30332
ge@fluent.com, suresh.menon@ae.gatech.edu

Lean perfectly premixed flame propagation in a swirling flow dump combustor is studied. The emphasis is on flame propagation in the Broken Reaction-Zone (BRZ), where the reaction zone thickness (δ_F) is larger than the Kolmogorov scale (η). The Linear-Eddy Mixing (LEM) model is used to simulate subgrid interactions between the flame structure and the unresolved turbulent structures within the framework of a large-eddy simulation (LES) approach. A real case scenario is studied: the propagation of a lean premixed flame in a dump combustion chamber where heat losses at the walls are taken into account via the use of a simple heat loss model. Results show flame lift-off, caused by flame quenching, for low equivalence ratio (Φ=0.45). The dynamics of flame quenching, and the subsequent flame lift-off, can be linked to the natural combustion chamber dynamics. The frequency of flame lift off is equal to the half-first longitudinal combustion chamber oscillation mode.

I. Introduction

Since the early 90's, gas turbine based ground power generation is considered an environmentally-friendly alternative to the more polluting coal-burning power plants. As large investments are made to transport and distribute natural gas in a liquid form (Liquid Natural Gas, a.k.a. LNG), the number of gas turbine power plants that will enter into service will soar in the next few decades. Independently to the development of LNG technologies, gasified coal (*syngas*) is also considered as a possible fuel for gas turbine power plants, even though *syngas* is less energy-dense than natural gas. These state-of-the-art gas turbines use the Lean-Premix-Prevaporized (LPP) technology and are operated at an equivalence ratio that is only slightly higher than the lean extinction limit. Although it is often assumed that the turbulent combustion process taking place in these gas turbines is in the flamelet regime, where δ_F is larger than η, and the chemical time scale (τ_C) is smaller than the characteristic turbulent flow time scale (τ_F), other turbulent combustion regimes are also locally present. In regions of high turbulence, the smallest eddies can be smaller than the flame thickness. In this case, eddies penetrate the preheat zone, increase heat and species transport, and increase the flame thickness. Furthermore, experiments[1–3] have shown that very high level of turbulence can result in flame quenching, and that the stabilized flame can exhibit local extinction (quenching of a very small portion of the flame) without global extinction (quenching of a large portion in the flame creating a hole in the flame where unburnt reactants penetrate into the product region). Both local and global flame quenching are not fully understood. In theory, flame quenching is a direct result of the action of turbulent structures small and/or powerful enough to break-up the structure of the reaction zone, but this has never been formally demonstrated, neither by experiments nor by numerical simulations. Other factors such as reactants equivalence ratio distribution, combustion chamber geometry, heat losses, etc., all have to be considered when flame quenching is studied.

This work focuses on the numerical investigation of lean, swirl stabilized turbulent premixed flames with the objective to study flame quenching phenomena and its impact on the overall combustion process. In

*Consulting Engineer, Fluent, Inc.
†Professor, AIAA Associate Fellow

particular, we investigate the sensitivity of flame stability and lift-off to local heat losses.

In the next section the LES formulation along with the subgrid LEM closure employed is described. This model is denoted $LEMLES$, hereafter. In section III, the numerical implementation is presented. Then, in section IV, flame propagation is studied in a full scale combustion chamber with realistic operating conditions. Finally, conclusions are given in section V.

II. Mathematical Formulation

A. LES Formulation

The governing equations of motion for an unsteady, compressible, reacting, multi-species fluid are the Navier-Stokes equations describing the conservation of mass, momentum, total energy and N-species. In LES, the large scale motion is fully resolved on the computational grid using a time- and space-accurate scheme, and only the small scales are modeled. The separation between the large (resolved) and the small (unresolved) scales is determined by the grid size ($\overline{\Delta}$). The filtered Navier Stokes equations for mass, momentum, energy conservation and their closure are briefly described here sice further details can be found elsewhere.[4]

A Favre spatial top-hat filter (which is appropriate for the finite-volume scheme employed here) is employed to derive the LES equations.[5] Thus, any variable (f) is decomposed into a resolved quantity ($\widetilde{f}$) and a unresolved (quantity (f'') such that $f = \widetilde{f} + f''$. The resulting LES equations are:[4]

$$\begin{cases} \frac{\partial \overline{\rho}}{\partial t} + \frac{\partial \overline{\rho}\widetilde{u_i}}{\partial x_i} = 0 \\ \frac{\partial \overline{\rho}\widetilde{u_i}}{\partial t} + \frac{\partial}{\partial x_j}\Big[\overline{\rho}\widetilde{u_i}\widetilde{u_j} + \overline{p}\delta_{ij} - \overline{\tau_{ij}} + \tau_{ij}^{sgs}\Big] = 0 \\ \frac{\partial \overline{\rho}\widetilde{E}}{\partial t} + \frac{\partial}{\partial x_i}\Big[\Big(\overline{\rho}\widetilde{E} + \overline{p}\Big)\widetilde{u_i} + \overline{q_i} - \widetilde{u_j}\overline{\tau_{ji}} + H_i^{sgs} + \sigma_i^{sgs}\Big] = 0 \end{cases} \tag{1}$$

In the above equations, u_i is the i-th velocity component, ρ is the mass density, p is the pressure and $E = e + \frac{1}{2}(u_k^2 + k^{sgs})$ is the total energy. Here, e is the internal energy per unit mass computed as the sum of the sensible enthalpy and the chemical stored energy, and k^{sgs} is the sub-grid kinetic energy (defined below). Also, q_i is the heat flux vector and τ_{ij} is the viscous stress tensor, given by $\tau_{ij} = \mu\Big(\partial u_i/\partial x_j + \partial u_j/\partial x_i\Big) - \frac{2}{3}\mu\Big(\partial u_k/\partial x_k\Big)\delta_{ij}$. Here, μ is the molecular viscosity coefficient which is determined using the Sutherland's law.

In the LES equations, all the above variables appear in their filtered form, and many terms (with superscript sgs) require closure. Some simplifications are required as well. For example, the filtered viscous shear stress ($\overline{\tau_{ij}}$) and heat flux ($\overline{q_i}$) are approximated using the filtered velocity and filtered temperature. The unclosed terms that represent the effect of the unresolved motion on the resolved field are: τ_{ij}^{sgs}, H_i^{sgs} and σ_i^{sgs}, and are respectively, the sub-grid shear stress, the sub-grid heat flux and the sub-grid viscous stress. These terms are defined as follows:

$$\begin{cases} \tau_{ij}^{sgs} = \overline{\rho}\Big[\widetilde{u_i u_j} - \widetilde{u_i}\widetilde{u_j}\Big] \\ H_i^{sgs} = \overline{\rho}\Big[\widetilde{E u_i} - \widetilde{E}\widetilde{u_i}\Big] + \Big[\overline{p u_i} - \overline{p}\widetilde{u_i}\Big] \\ \sigma_i^{sgs} = \overline{\rho}\Big[\overline{u_j \tau_{ji}} - \widetilde{u_j}\overline{\tau_{ji}}\Big] \end{cases} \tag{2}$$

Note that the above equations do not include any species equations since they are handled in a different manner in LEMLES, as described later.

B. Subgrid Closure for Momentum and Energy Transport

The sub-grid stress τ_{ij}^{sgs} and the sub-grid heat flux H_i^{sgs} are closed using an eddy viscosity closure. This closure employs a non-equilibrium model for the sub0grid kinetic energy k^{sgs}. A transport equation is formally derived for k^{sgs} and solved along with the rest of the LES equations. Past studies[4,6–8] have demonstrated the ability and accuracy of this model.

The k^{sgs} transport model is given as:

$$\frac{\partial \overline{\rho} k^{sgs}}{\partial t} + \frac{\partial}{\partial x_i}\Big(\overline{\rho}\widetilde{u_i} k^{sgs}\Big) = P^{sgs} - D^{sgs} + \frac{\partial}{\partial x_i}\Big(\frac{\overline{\rho}\nu_T}{\sigma_k}\frac{\partial k^{sgs}}{\partial x_i}\Big) \tag{3}$$

Here, $k^{sgs} = \frac{1}{2}\Big[\widetilde{u_k^2} - \widetilde{u_k}^2\Big]$ and $\sigma_k = 1$.

In the above equation, $P^{sgs} = -\tau_{ij}^{sgs}\frac{\partial \widetilde{u_i}}{\partial x_j}$ and $D^{sgs} = C_\epsilon \overline{\rho}(k^{sgs})^{3/2}/\overline{\Delta}$ represent respectively, the production and the dissipation of the sub-grid kinetic energy. The sub-grid stress is then obtained as:

$$\tau_{ij}^{sgs} = -2\overline{\rho}\nu_T\Big(\widetilde{S_{ij}} - \frac{1}{3}\widetilde{S_{kk}}\delta_{ij}\Big) + \frac{2}{3}\overline{\rho}k^{sgs}\delta_{ij} \tag{4}$$

where the sub-grid eddy viscosity is given by $\nu_T = C_\nu(k^{sgs})^{1/2}\overline{\Delta}$.

In this formulation, the two model coefficients $C_\nu = 0.067$ and $C_\epsilon = 0.916$. These constants were established earlier using theoretical and numerical studies of high-Re stagnation point premixed flames.[9,10] A localized dynamic approach is also available[4,7,8] and will be considered in a future study. However, the overall results reported here are not expected to be very sensitive to this issue.

The subgrid enthalpy flux is closed using the same eddy viscosity approach:

$$H_i^{sgs} = -\frac{\nu_T}{Pr_T}\frac{\partial \widetilde{h}}{\partial x_i} \tag{5}$$

where $\widetilde{h}$ is the specific enthalpy and Pr_T is a turbulent Prandtl number assumed to be unity at present.

Closure of other subgrid terms are also required in the energy equation. For example,

$$\overline{q_i} = -\overline{\kappa}\frac{\partial \widetilde{T}}{\partial x_i} - \overline{\rho}\sum_{k=1}^{N}\widetilde{h_k}\frac{\partial \widetilde{Y_k}}{\partial x_i} + \sum_{k=1}^{N} q_{ik}^{sgs} \tag{6}$$

where q_{ik}^{sgs} represents the heat transfer via turbulent convection of species. This term is neglected in this study. The filtered equation of state is used to compute the filtered pressure:

$$\overline{p} = \overline{\rho}R_u\sum_{m=1}^{N}\left[\frac{\widetilde{Y_m}}{W_m}\widetilde{T} + \frac{\widetilde{Y_m T} - \widetilde{Y_m}\widetilde{T}}{W_m}\right] \tag{7}$$

At present ${T_m}^{sgs} = \frac{\widetilde{Y_m T} - \widetilde{Y_m}\widetilde{T}}{W_m}$ is neglected based on earlier studies.[11,12]

C. Subgrid Closure for Scalar Transport ($LEMLES$)

In conventional LES, the scalar equations are solved along with the LES equations for mass, momentum and energy using a sub-grid eddy diffusivity closure. Many closures for the filtered reaction rate can be used with this approach but all of them have their strengths and weaknesses. In particular, closure of sub-grid molecular mixing and reaction kinetics can be problematic when multi-species (with widely different molecular diffusivity) finite-rate kinetics have to be studied. In $LEMLES$, scalars conservation equations are solved using a Eulerian-Lagrangian approach that avoids using LES spatial filtering of the scalar equations.

Although details of this procedure has been given elsewhere,[13,14] we summarize some of the salient features of this method. Rather, molecular diffusion, small- and large-scale turbulent convection, and chemical reaction are all modeled separately, but concurrently at their respective time scales. To briefly describe this model mathematically, we split the velocity field as: $u_i = \tilde{u_i} + (u_i')^R + (u_i')^S$. Here, $\tilde{u_i}$ is the LES-resolved velocity field, $(u_i')^R$ is the LES-resolved subgrid fluctuation (obtained from k^{sgs}) and $(u_i')^S$ is the unresolved subgrid fluctuation. Then, consider the *exact* species equation (i.e., without any explicit LES filtering) for the k-th scalar Y_k written in a slightly different form as:

$$\rho\frac{\partial Y_k}{\partial t} = -\rho[\tilde{u_i} + (u_i')^R + (u_i')^S]\frac{\partial Y_k}{\partial x_i} - \frac{\partial}{\partial x_i}(\rho Y_k V_{i,k}) + \dot{w}_k \tag{8}$$

In LEMLES, the above equation is rewritten as:

$$\frac{{Y_k}^* - {Y_k}^n}{\Delta t_{LES}} = -[\tilde{u_i} + (u_i')^R]\frac{\partial {Y_k}^n}{\partial x_i} \tag{9}$$

$$Y_k{}^{n+1} - Y_k{}^{*} = \int_t^{t+\Delta t_{LES}} -\frac{1}{\rho}[\rho(u_i')^S \frac{\partial Y_k{}^n}{\partial x_i} + \frac{\partial}{\partial x_i}(\rho Y_k V_{i,k})^n - \dot{w}_k^n]dt' \tag{10}$$

Here, Δt_{LES} is the LES time-step. Equation (9) describes the large-scale 3D LES-resolved convection of the scalar field, and is implemented by a Lagrangian transfer of mass across the finite-volume cell surfaces.[9,15] Equation (10) describes the subgrid LEM model, as viewed at the LES space and time scales. The integrand includes four processes that occur within each LES grid, and represent, respectively, (i) subgrid molecular diffusion, (ii) reaction kinetics, (iii) subgrid stirring, and (iv) phase change of the liquid fuel. These processes are modeled on a 1D domain embedded inside each LES grid where the integrand is rewritten in terms of the subgrid time and space scales.

The LEM domain is a one-dimensional line and LEM domain is embedded in every LES cell. The number of LEM cells per LES cells is N^{LEM}, which is a function of the LES resolution and the level of turbulence. The length of the LEM domain (L^{LEM}) is approximated as $L^{LEM} = \frac{\left(\Delta V_{LES}\right)^{\frac{1}{3}}}{N^{LEM}}$ where ΔV_{LES} is the volume of the LES cell. A uniform grid is used in each LEM cell. The LEM domain governing equations are shown below.

$$\begin{aligned} \rho^{LEM}\frac{\partial Y_k^{LEM}}{\partial t} \quad &+ \quad F_k^{stir} + \underbrace{\frac{\partial}{\partial s}\Big(-\rho_{LEM} D_k \frac{\partial Y_k^{LEM}}{\partial s}\Big)}_{I} \\ &= \quad \underbrace{\dot{w}_k W_k}_{II} \end{aligned} \tag{11}$$

$$\begin{aligned} \rho^{LEM} C_P \frac{\partial T^{LEM}}{\partial t} \quad &+ \quad F_T^{stir} - \underbrace{\sum_{k=1}^{N} \rho C_{P,k} D_k \Big(\frac{\partial Y_k^{LEM}}{\partial s}\Big)\Big(\frac{\partial T^{LEM}}{\partial s}\Big)}_{III} \\ &- \quad \underbrace{\frac{\partial}{\partial s}\Big(\overline{\kappa}\frac{\partial T^{LEM}}{\partial s}\Big)}_{IV} = \underbrace{-\sum_{k=1}^{N} h_k \dot{w}_k W_k}_{V} \end{aligned} \tag{12}$$

Here, Y^{LEM}, T^{LEM} and ρ^{LEM} are the sub-grid LEM species mass fraction, temperature and density, respectively. Species molecular diffusion (I), chemical reactions (II), diffusion of heat via species molecular diffusion (III), heat diffusion (IV), and chemical reaction heat release (V) are solved locally on the 1D line. Here, s is the coordinate along the LEM line and this line is oriented in the direction of maximum strain, i.e. perpendicular to the flame surface. Also, D_k is the molecular diffusion coefficient of the $k-th$ species, $C_{p,k}$ is the specific heat coefficient per unit mass of the $k-th$ species, D_k is the diffusion coefficient of the $k-th$ species and W_k is the molecular weight of the $k-th$ species. Finally, F_k^{stir} and F_T^{stir} are terms that represent the action of sub-grid turbulence.

In the LEMLES approach, we assume that the sub-grid pressure p^{LEM} is the same as the LES pressure p^{LES}. This approximation is reasonable as long as there is no significant compressibility (e.g., shock waves) within the sub-grid. the sub-grid mixture density ρ^{LEM} is obtained using the sub-grid equation of state:

$$p^{LEM} = \rho^{LEM} T^{LEM} R_u \sum_{k=1}^{N} \frac{Y_k^{LEM}}{W_k} \tag{13}$$

The exact $LEMLES$ closure is similar to the closure in PDF methods[16] except that, unlike in PDF methods, molecular diffusion (and hence, differential diffusion) effects can also be included in the $LEMLES$. As in PDF methods, the large-scale transport is modeled as a Lagrangian transport of the scalar fields across LES cells and the sub-grid turbulent stirring is modeled. In PDF methods, the Curl's coalescence-dispersion mixing model is often employed to model turbulent mixing, whereas in $LEMLES$, small-scale turbulent stirring is implemented using a scalar rearrangement process (denoted F_k^{stir} and F_T^{stir} above) that mimics the action of an eddy upon the scalar field.[17] The location of this stirring event is chosen from a uniform distribution and the frequency of stirring is derived from $3D$ inertial range scaling laws derived from Kolmogorov's hypothesis as:

$$\lambda = \frac{54}{5}\frac{\nu Re_{\overline{\Delta}}}{C_\lambda \overline{\Delta}^3}\frac{[(\overline{\Delta}/\eta)^{5/3}-1]}{[1-(\eta/\overline{\Delta})^{4/3}]} \tag{14}$$

C_λ represent the scalar turbulent diffusivity and is determined as 0.067. The eddy size (l) is chosen from the following PDF:

$$f(l) = \frac{(5/3)l^{-8/3}}{\eta^{-5/3} - \overline{\Delta}^{-5/3}} \tag{15}$$

where $\eta = N_\eta \overline{\Delta} Re_{\overline{\Delta}}^{-4/3}$. The empirical constant N_η reduces the effective range of scales between the integral length scale and η but does not change the turbulent diffusivity ($N_\eta \in [1.3;10.78]$).

It has been demonstrated that these turbulent scaling laws correctly predict the growth of the flame surface area under the influence of turbulent strain. Note that this model does not require any change when the flame type (premixed or diffusion flame) or the combustion regime (flamelet, Thin Reaction-Zone or Broken-Reaction-Zone regimes) changes. This ability has been demonstrated in the past[18,19] and it is this ability that we believe is crucial to deal with complex phenomenon such as LBO.

Volume expansion due to heat release is also included in the LEM domain. When combustion (therefore, heat release) occurs, the volume of the LEM cell is expanded according to the change in density caused by the increase in sub-grid temperature (the mass of the LEM cell being constant). Once this is done for all LEM cells, all the LEM domains are re-gridded such that all LEM cell have the same volume. Some spurious diffusion can occur during this process, however, since the sub-grid evolution occurs at a very small time interval very few cells are effected and therefore, this effect is considered insignificant.

The transport of the subgrid scalar field, Equation (9) is carried out across the LES cell faces in a Lagrangian manner. This transport is achieved using a "splicing" technique. Splicing involves the transfer of LEM cells between the LES control volumes accounting for the mass-flux across each LES cell-faces. The mass-flux on each of the six control-surface (for hexahedral control volume) is first sorted in an ascending order following sign-convention of positive influx and negative efflux. The number of LEM cells is then determined based on the amount of mass flux that needs to be transported across each LES cell face. At many locations, fractional LEM cells have to be transported to maintain mass conservation. Mass transported out of the LEM domain is taken out from one end of the 1D domain and mass transport in, is added to the other end of the 1D domain. Further details are given elsewhere[9,13,15]

Conservation of mass, momentum and energy (at the LES level) and conservation of mass, energy and species (at the LEM level) are strongly coupled.[14] Chemical reaction at the LEM level determines heat release and thermal expansion at the LEM level, which at the LES level generates flow motion that, in turns, transports the species field at the LEM level. Full coupling is maintained in the $LEMLES$ to ensure local mass conservation.

III. Numerical Setup and Conditions

A. Combustor Geometry and Test Conditions

Combustion inside a 3D dump combustor that consists of a circular inlet pipe opening into a larger circular combustor, is simulated. Dimensions are given in Fig. 1. The grid resolution is 140x75x81 for the cylindrical grid that fits the combustion chamber geometry and 140x21x21 for the Cartesian grid that is used to resolve the centerline region. The inflow pressure is 6 bar, the inflow temperature is 644 K and the reacting mixture is a premixed mixture of methane and air. Operating conditions are chosen to match approximately the General Electric LM6000 combustion chamber condition.

The flow enter in a swirling manner and is characterized by a Swirl number of 1.1 at the inflow. The incoming equivalence ratios considered in this study are $\Phi = 1.0$ and $\Phi = 0.45$. Characteristic based inflow and outflow conditions are employed along with adiabatic, non-catalytic and no-slip walls. As noted later, to study the effect of heat loss, some changes are explicitly incorporated as described later. Inflow profiles are chosen to match the flow rate and to provide the proper swirl number. A small 10% turbulence quantity is also added to the inflow to initial k^{sgs}.

B. *LEM* Resolution

The choice of the number of *LEM* cells per *LES* cell is a compromise between the need to resolve all turbulent and chemical length scales, and the computational cost. In the present study, we use 18 *LEM* cells per *LEM* line. Figure 2 (a) shows the typical distribution of the *LES* subgrid velocity fluctuations (u') in the combustion chamber. For each level of turbulence (i.e. for each u'), a *PDF* of the eddy size can be computed.[13] Using this eddy size *PDF* distribution, the expected eddy size ($\overline{L}$) is computed for all values of u', and is expressed as the number of *LEM* cells needed to resolve it. A minimum of six *LEM* cells is needed to resolve an eddy and all eddies that are larger than six *LEM* cells are fully resolved. Figure 2 (a) shows that around 97% of the sub-grid eddies present in the combustion chamber are resolved (Domain (A)).

It is also of great interest to evaluate the resolution of the LEM line with regards to the resolution of the flame/eddy interactions. Figure 2 (b) shows the *CDF* distribution of the eddy size and the Karlovitz number ($Ka=(\delta_F/\eta)^2$) as a function of u' and for Φ=0.5. Figure 2 (b) shows that both the flamelet and the *TRZ* regime are fully resolved (domain I). Six percent of the domain has a level of turbulence corresponding to the *BRZ* regime (domains II and III). In domain II, all scales relevant to the flame/eddy interactions are resolved on the *LEM* level, whereas these interactions are under-resolved in domain III. It is important to note that Fig. 2 (b) shows that the flame does not propagate in the flamelet regime (Ka<1). This is due to the fact that only *LES* sub-grid turbulent scales are considered in Figs. 2 (a) and 2 (b). For low level of u', the frequency of occurrence of sub-grid eddies is negligible and only *LES* resolved eddies affect the flame front. Since *LES* resolved eddies are larger than the flame front, therefore, for low level of turbulence, the flame propagates in the flamelet regime.

The flame front thickness is 0.15 mm and 1.2 mm for Φ=1.0 and Φ=0.45 (equivalence ratio used for the study of flame propagation), respectively. In the flame region, the typical *LES* resolution is 0.45 mm. Thus, on average, with 18 *LEM* cells per *LES* cell, the flame is resolved using approximately 5 *LEM* cells for Φ=1.0 and 40 *LEM* cells for Φ=0.45.

C. Efficient Computation of the Chemical Rates

In the current study, both global and multi-step, reduced finite-rate kinetics are used within LEMLES. The mass reaction rate is computed using either a 5-species, 1-step chemical mechanism:[20]

$$CH_4 + 2(O_2 + 3.76N_2) \rightleftharpoons CO_2 + 2H_2O + 7.52N_2 \tag{16}$$

or a 8-species - 4-steps chemical mechanism:[21]

$$\begin{aligned} CH_4 + 2H + H_2O &\rightleftharpoons CO + 4H_2 \\ CO + H_2O &\rightleftharpoons CO_2 + H_2 \\ 2H + M &\rightleftharpoons H_2 + M \\ O_2 + 3H_2 &\rightleftharpoons 2H + 2H_20 \end{aligned} \tag{17}$$

It is well known that finite-rate kinetics evaluation is computationally very expensive and typically, is over 95% of the total cost. Direct integration of the stiff kinetics using the *DVODE* (Double precision and Variable coefficient ODE) solver is prohibitive. Table 1 summarizes estimates for *LEMLES* when normalized to the computational cost of *LES* simulations using the $G-equation$ model.[22] *LEMLES* simulations without kinetics is only marginally expensive but when using the *DVODE* solver are 28 and 80 times more expensive for the 5-species and the 8-species mechanism, respectively. Analysis shows that the computational cost rate integration is over 90% of the total computational cost. This is not acceptable and alternate methods are needed.

Earlier studies had shown that the In-Situ-Adaptive-Tabulation (*ISAT*)[23] method that first stores the computed rates and then retrieves them later has the potential of reducing the computational time considerable. A speed-up of around 30 was noted earlier when using a more detailed 16-species mechanism.[18] However, when a limited number of species is used (either 5 or 8, as in this study), no significant gain was observed using ISAT and therefore, is not utilized here.

A simple, cost effective and accurate method for the computation of the reaction rates was designed. This method is valid for both chemical mechanisms used here. When the $DVODE$ solver is used, the computation of the reaction rate per LES time step is performed by dividing the actual LES computational time step (Δt_{LES}), and performing a direct computation of the reactions rate over this smaller time step (Δt_{CHEM}), which is computed by the $DVODE$ solver. It was found that for the chemical mechanisms used in this study, the time step computed by the $DVODE$ solver is fairly constant (Δt_{CHEM}=$\Delta t_{LES}/K$) and K can be determined by studying the chemical mechanism on a simple $1D$ problem. By using a fixed Δt_{CHEM} the $LEMLES$ computation speeds up by a factor of 4 (see Table 1) with an error of less than one percent for both mechanism.

Model	Time (compared to $GLES$)
$LEMLES$ - 5-species - No reaction	3
$LEMLES$ - 5-species - Reaction (Δt_{CHEM}=$\Delta t_{LES}/3$)	7
$LEMLES$ - 5-species - Reaction (DVODE)	28
$LEMLES$ - 8-species - No reaction	6
$LEMLES$ - 8-species - Reaction (Δt_{CHEM}=$\Delta t_{LES}/5$)	28
$LEMLES$ - 8-species - Reaction (DVODE)	80

Table 1. Comparison of the computational cost of different approaches for the 5- and 8-species mechanisms. The cost using a level set approach ($G-equation$ model) is used as a reference.

D. Parallel Implementation and Performance

It is evident from the above discussion that a large amount of computational resource is needed for these types of simulations. Both run time (number of hours) and memory requirements are severe. The current LEMLES solver is fully implemented in parallel using the MPI libraries and it quite efficient on a large number of processors. The sub-grid LEM closure is particularly suited for parallel simulation since many calculations in the LEM model are local.

The performance of the solver used in this study is evaluated and the speed-up is presented in Figure 3. Computational times were obtained using the $LEMLES$ approach with 18 LEM cells per LEM domain, and with the 1-step chemical mechanism. Computational times are plotted as a function of the number of LES cells contained in each grid sub-elements, i.e. the number of computational points per processor. As a reference, ideal computation times are plotted. Computational times are said to be 'ideal' when a increase of the number of processors by a factor of N leads to a decrease in computational time by a factor of N. As shown in Figure 3, the behavior of the program is close to the ideal behavior primarily because, in the $LEMLES$ model, a large fraction of the computational cost is due to the computation of the reaction rates. Thus, a substantial reduction in the turnaround time can be achieved if the number of processors are increased. This excellent scalability suggests that the large increase in cost of LEMLES with finite-rate kinetics (shown in Table 1) can be handled by using a larger number of processors. Furthermore, with increase in processor speed that is continuously occurring now-a-days, it is anticipated that such simulations will be feasible with a practical turn-around-time of 1 week or less on large massivelly parallel systems in the near future.

IV. Results and Discussion

A. Heat Loss Modeling

Simulations using adiabatic walls are first conducted using the current LEMLES model. It was determined that even the chosen lean case shows no sign of flame quenching and the flame remains attached to or near the inlet lip. Such stable flame holding has been seen in many past LES studies using similar combustors.[14,24] Past studies shows that even during onset of combustion instability (i.e., growth of large-amplitude, low-frequency pressure oscillations), the premixed flame remains attached to the inlet wall (although it can move upstream into the inlet showing local flashback). However, no quenching is observed.

However, in practical systems, heat loss occurs at the walls of the combustion chamber since they are not

adiabatic. The wall material cannot withstand the high product temperature and typically, the walls are cooled and/or air is injected via holes in the combustion chamber to create a protective colder layer of gases. Considering wall related heat losses is not practical in *LES* of combustion chambers at this time because to do so, it is necessary to fully resolve the wall thermal boundary layer. However, one can simulate heat loss effect by directly including its effect locally. Following the study of Poinsot et *al.*,[25] heat loss is included in the energy balance in the LEM domain in the following linear form:

$$\frac{dT_{HL}}{dt} = \frac{h}{\rho C_P}(T - T_1) \tag{18}$$

where T_1 is the reactant temperature. This term is added to the sub-grid energy equation, Eq. 18. The coefficient h is defined as follow:

$$h = \lambda S c^2 \left(\frac{S_L}{\nu}\right)^2 \frac{c}{\beta} \tag{19}$$

where $\lambda = \mu C_P / P_r$, β is the reduced activation energy,[26] and c is a dimensionless heat-loss coefficient. Heat loss is taken into account only in the post-flame region and is a direct function of the product temperature.

Figures 4(a)-(c) illustrates the behavior of the temperature field for c=0 (Fig. 4 (a)), c=10^{-4} (Fig. 4 (b)) and c=10^{-3} (Fig. 4 (c)). For medium heat loss (c=10^{-4}), an equilibrium exists between the heat released at the flame front and the heat loss, whereas for the case with large heat loss (c=10^{-3}) such an equilibrium does not exist, and the flame quenches. This latter case is not of current interest and therefore, the value of c is taken as 10^{-4}. It is noted, this chosen value need not be universal and further study is still needed.

Heat loss in the current study is also not implemented along all the combustor walls. Rather, it is turned on only in the region close to the edge formed by the expansion of the inflow pipe inside the combustion chamber. This is a region of around 1.5 mm radius from this edge. As a result, the final value of c is given by: $c = f(r)c^*$ where c^*=10^{-4} and $f(r)$=$max((1 - r/1.5), 0)$ with r taken as the distance from the chosen point to the edge of the inflow pipe. Again, this choice is rather ad hoc but is used here primarily to assess the importance of heat loss on the flame holding mechanism in such combustors. Future studies will attempt to revisit this issue using a more generalized isothermal wall condition. However, in order to do this it will be necessary to know exactly the wall temperature or heat flux condition, either of which is not that easy to obtain in real systems.

Some additional simplifications are used as well to implement this heat loss model. Heat loss is only implemented at the *LEM* level during the sub-grid reaction-diffusion simulation within each LES cell, and are neglected at the *LES* level. It is assumed at present, that heat loss in the local chosen region has only a limited *direct* influence on the LES-resolved velocity field. However, since the sub-grid scalar fields are modified by local heat loss, there is an indirect impact on the LES-resolved motion due to changes to the filtered species (obtained from the LEM domains) used in the closure of the LES conservation of energy and equation of state. Nevertheless, this is still an area for further research.

B. Main Flow Features

The time-averaged axial velocity profiles are shown in Fig.5 (a), for $\Phi = 1.0$ and in Fig.5 (b), for $\Phi = 0.45$. The local region of reverse flow are also shown in these figures. Figure 6 shows the time-averaged swirl number for both equivalence ratio as a function of the distance from the inflow. The sudden drop in the swirl number is due to the change in radius used in the computation of the swirl number (the radius changes from the radius of the inflow pipe to the radius of the combustion chamber).

Both the axial velocity and swirl number profile along the centerline are very similar for Φ=0.45 and Φ=1.0. For both cases, two recirculation regions are present. The first one is located downstream of the dump plane and is created by the sudden expansion of the inflow pipe inside the combustion chamber. The reattachment length of this recirculation region is approximately equal to the length of the step formed by the dump plane. The second one, of oval shape, is located in the centerline region and is created by the swirling flow. The length of this region is approximately equal to the diameter of the combustion chamber and the average maximum negative flow velocity is 30 ms^{-1}. Both recirculation regions stabilize the flame by recirculating high temperature products upstream and towards the flame front. The vortex breakdown bubble is responsible for the tulip-like shape of the flame for Φ=1.0.

C. Flame Quenching

Evidence of flame propagation in the BRZ regime is given in Fig. 7, which shows an iso-surface of $Ka = 100$. This is done using an instantaneous field (a time-averaged Karlovitz number field has no relevance). As shown in Figure 7, a portion of the domain is characterized by $Ka > 100$, which indicates that in this region, the flame propagates in the BRZ regime. Further analysis suggests that combustion occurs in all the regimes: flamelet, TRZ and BRZ, depending upon the local conditions in space and time. As noted earlier, in LEMLES there is no need to adjust the model based on local conditions and the model automatically adjusts to the changes in the local conditions.

When heat loss is introduced, local flame quenching occurs for the lean case, and be seen when $\dot{w}_{CH_4}$ is plotted as a function of $\widetilde{Y_{CH_4}}$. Figure 8 (a) corresponds to $\Phi = 1.0$ and Fig. 8 (b) corresponds to $\Phi = 0.45$. For $\Phi = 1.0$, results show that the fuel reaction rates are spread over a large range but no flame quenching is observed. The spreading of the scatter points is mainly a result of the modeled heat loss but no values close to zero are seen. However, for $\Phi = 0.45$, values of $\dot{w}_{CH_4}$ can reach 0 for all values of Y_{CH_4}, hence proving that some portion of the flame are quenched.

The above results are obtained using the 8-species mechanism. It is anticipated that with proper modeling of the heat loss parameters, a similar result can be obtained using the 5-species mechanism. Figure 8 (b) clearly indicates that the introduction of the heat loss does not fully prevent combustion. Rather, heat loss perturbs the flame propagation and its location, and depending upon the sub-grid processes quenches or does not quench the flame front.

It is noted further that in the present study, reaction kinetics were not modified and only wall conditions were changed within the LEMLES. Since finite-rate kinetics is included without requiring any closure, heat loss directly effects the reaction kinetics, and this in turn, impacts thermal expansion effect and eventually the flow field. It is not clear at present if a conventional LES using a eddy diffusivity closure and a "modeled" filtered reaction rate approach (e.g., Eddy breakup or assumed PDF, etc) will respond in a similar manner to the heat loss modeled as a wall condition.

D. Dynamics of Flame Lift-off

The sum of all local fuel reaction rates (in the region from the dump plane to 7.5 mm downstream of the dump plane) is computed as a function of time and is plotted in Fig. 9. The maximum absolute value of the sum is used to normalize the data. The first mode of the oscillations is extracted. The flame is lifted-off when the normalized sum of the reaction rate is close to 0. The flame is attached to the inflow pipe lip when the normalized sum of the reaction rate is close to -1. The first mode of the oscillations has a frequency of approximately 1 kHz. The flame quenching frequency matches the longitudinal half quarter mode of the combustion chamber.

To gain more insight into the flame lift-off dynamics, reaction rate iso-surface is shown in Fig. 10 at four different equidistant times within the 1 ms time span. Analysis shows that acoustics in the combustion chamber also plays an important role in the observed dynamics. Pressure (acoustic) waves in the combustion chamber travel in both directions during the combustion process. When a pressure disturbance propagates downstream axial flow is enhanced and as the heat loss builds up near the dump plane, the flame locally quenches and lifts-off. When the pressure wave propagates upstream axial motion is slowed down and hot products are pushed more to the dump plane region. This upstream transport of hot products counteract the action of the heat loss. Therefore, the flame front is not quenched and the flame remains attached to the dump plane. This is similar to the compact flame regime observed by Sommerer et *al*..[27] Due to the transient nature of this process, periodic attachment and lift-off occurs, showing the importance of heat loss (as noted earlier, without this heat loss model the flame remains attached for the same operating conditions).

V. Conclusion

Flame quenching is successfully simulated for lean premixed flame and it is shown that this occurs only when heat loss is taken into account. The dynamics of flame lift-off is coupled to the natural dynamics of the combustion chamber. Future work must include a better estimate of the amount of heat losses at the wall. Experimental data have to be available, and a wall flux heat loss model more accurate that the current model is needed for more accurate modeling of this effect.

Acknowledgements

This work is partially supported by General Electric Global Research under a US Department of Energy contract and by Army Research Office. Some of the simulations were conducted at the High Performance Computing Center at ERDC, MS and this support is gratefully acknowledged.

References

[1]Buschmann, A., Dinkelacker, F., Schaefer, T., Schaefer, M., and Wolfrum, J., "Measurement of the Instantaneous Detailed Flame Structure in Turbulent Premixed Combustion," *Twenty-Sixth Symposium (International) on Combustion*, 1996, pp. 437–445.

[2]Mansour, M., Peters, N., and Chen, Y., "Investigation of Scalar Mixing in the Thin Reaction Zones Regime using a simultaneous CH-LIF/Rayleigh Laser Technique," *Proceedings of the Combustion Instutute*, Vol. 27, 1998, pp. 767–773.

[3]Dinkelacker, F., Soika, A., Most, D., Hofmann, D., Leipertz, A., Polifke, W., and Doebbeling, K., "Structure of Locally Quenched Higly Turbulent Lean Premixed Flames," *Twenty-Seventh Symposium (International) on Combustion*, 1998, pp. 857–865.

[4]Kim, W.-W., Menon, S., and Mongia, H. C., "Large-Eddy Simulation of a Gas Turbine Combustor Flow," *Combustion Science and Technology*, Vol. 143, 1999, pp. 25–62.

[5]Erlebacher, G., Hussaini, M. Y., Speziale, C. G., and Zang, T. A., "Toward the Large-Eddy Simulation of Compressible Turbulent Flows," *Journal of Fluid Mechanics*, Vol. 238, 1992, pp. 155–185.

[6]Menon, S., Yeung, P.-K., and Kim, W.-W., "Effect of Subgrid Models on the Computed Interscale Energy Transfer in Isotropic Turbulence," *Computers and Fluids*, Vol. 25, No. 2, 1996, pp. 165–180.

[7]Kim, W.-W. and Menon, S., "A New Incompressible Solver for Large-Eddy Simulations," *International Journal of Numerical Fluid Mechanics*, Vol. 31, 1999, pp. 983–1017.

[8]Kim, W.-W. and Menon, S., "Numerical Simulations of Turbulent Premixed Flames in the Thin-Reaction-Zones Regime," *Combustion Science and Technology*, Vol. 160, 2000, pp. 119–150.

[9]Chakravarthy, V. and Menon, S., "Large-Eddy Simulations of Turbulent Premixed Flames in the Flamelet Regime," *Combustion Science and Technology*, Vol. 162, 2000, pp. 1–48.

[10]Chakravarthy, V. and Menon, S., "Subgrid Modeling of Premixed Flames in the Flamelet Regime," *Flow, Turbulance and Combustion*, 2001.

[11]Fureby, C., "Large-Eddy Simulation of Turbulent Anisochoric Flows," *AIAA Journal*, Vol. 33, No. 7, 1995, pp. 1263–1272.

[12]Veynante, D., Piana, J., Duclos, J. M., and Martel, C., "Experimental analysis of flame surface density models for premixed turbulent combustion," *Twenty-Sixth Symposium (International) on Combustion*, The Combustion Institute, Pittsburgh, PA, 1996, pp. 413–420.

[13]Menon, S., McMurtry, P., and Kerstein, A. R., "A Linear Eddy Mixing Model for Large Eddy Simulation of Turbulent Combustion," *LES of Complex Engineering and Geophysical Flows*, edited by B. Galperin and S. Orszag, Cambridge University Press, 1993.

[14]Sankaran, V., Porumbel, I., and Menon, S., "Large-Eddy Simulation of a Single-Cup Gas Turbine Combustor," *AIAA-2003-5083*, 2003.

[15]Menon, S. and Calhoon, W., "Subgrid Mixing and Molecular Transport Modeling for Large-Eddy Simulations of Turbulent Reacting Flows," *Proceedings of the Combustion Institute*, Vol. 26, 1996, pp. 59–66.

[16]Pope, S. B., "PDF Methods for Turbulent Reactive Flows," *Progress in Energy and Combustion Science*, 1985, pp. 119–192.

[17]Kerstein, A. R., "Linear-Eddy Model of Turbulent Transport II," *Combustion and Flame*, Vol. 75, 1989, pp. 397–413.

[18]Sankaran, V. and Menon, S., "The Structure of Premixed Flame in the Thin-Reaction-Zones Regime," *Proceedings of the Combustion Institute*, Vol. 28, 2000, pp. 203–210.

[19]Eggenspieler, G. and Menon, S., "Modeling of Pollutant Formation near Lean Blow Out in Gas Turbine Engines," *Direct and Large Eddy Simulation V*, 2003.

[20]Westbrook, C. K. and Dryer, F. L., "Simplified Reaction Mechanisms for the Oxidation of Hydrocarbon Fuels in Flames," *Combustion Science and Technology*, Vol. 27, 1981, pp. 31–43.

[21]Card, J. M., Chen, J. H., Day, M., and Mahalingam, S., "Direct Numerical Simulation of Turbulent Non-Premixed Methane-Air Flames Modeled with Reduced Kinetics," *Studying turbulence using Numerical Simulation Databases - V*, 1994, pp. 41–54.

[22]Peters, N., *Turbulent Combustion*, Cambridge Monographs on Mechanics, 2000.

[23]Pope, S., "Computationally Efficient Implementation of Combustion Chemistry Using in Situ Adaptive Tabulation," *Combustion Theory Modelling*, Vol. 1, 1997, pp. 41–63.

[24]Stone, C. Menon, S., "Adaptive swirl control of combustion instability in gas turbine combustors," *Proceedings of the Combustion Institute*, Vol. 29, 2002, pp. 155–160.

[25]Poinsot, T., Veynante, D., and Candel, S., "Quenching processes and premixed turbulent combustion diagrams," *Journal of Fluid Mechanics*, Vol. 228, 1991, pp. 561–606.

[26]Williams, F. A., *Combustion Theory*, The Benjamin/Cummings Publishing Company, Inc., 2nd ed., 1985.

[27]Sommerer, Y., Galley, D., Poinsot, T., Ducruix, S., Lacas, F., and Veynante, D., "Large Eddy Simulation and Experimental Study of Flashback and Blow -Off in a Lean Partially premixed Swirler Burner," *Journal of Turbulence*, Vol. 5, 2004.

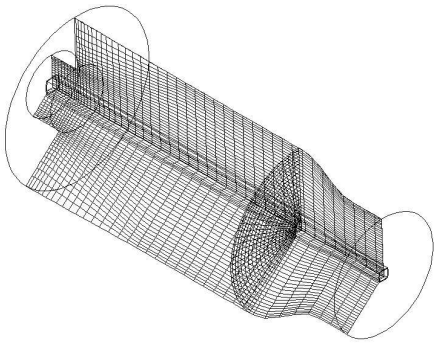

Figure 1. General view of the computational domain. The total combustion chamber length is 0.21m and the length of the inflow pipe is 0.015m. The radius of the combustion chamber and the inflow pipe are 0.045m and 0.017m, respectively.

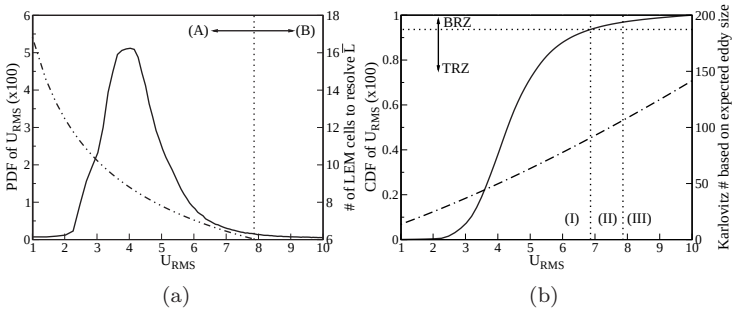

(a) (b)

Figure 2. Typical resolution at the LEM level of all relevant sub-grid eddies and combustion regimes. (a) PDF distribution of the sub-grid velocity fluctuations u' $(-)$ and expected eddy size $\overline{L}$ $(- \cdot\cdot -)$ as a function of u'. (b) CDF distribution of the subgrid velocity fluctuations u' $(-)$ and Karlovitz number $(- \cdot\cdot -)$ associated with the expected eddy size $\overline{L}$.

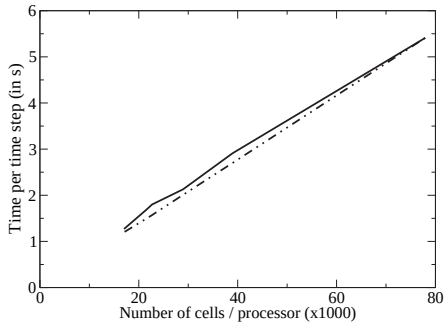

Figure 3. Scalability of the LEMLES approach. Time needed to perform one LES iteration as a function of the number of LES points per processor. The ideal speed-up uses the larger time per iteration as a reference and assumes that a reduction of the number of cells per processors by a factor f leads to a decrease in the computational time per iteration by the same factor f (Solid line: speed-up of the LEMLES solver; dashed line: ideal speed-up.)

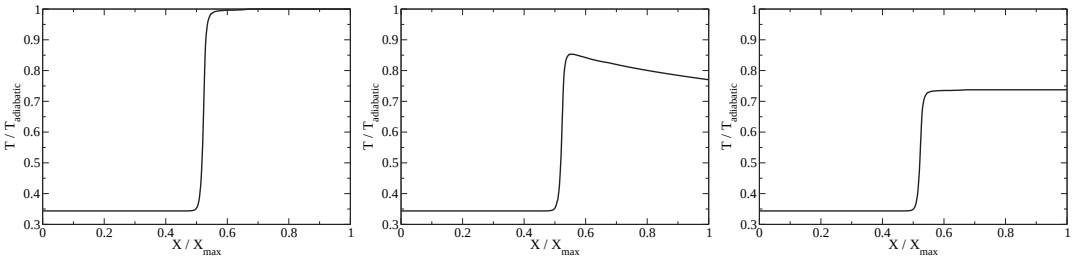

(a) c=0 (b) c=10^{-4} (c) c=10^{-3}

Figure 4. One-dimensional flame normalized temperature profiles for different values of the heat loss coefficient c.

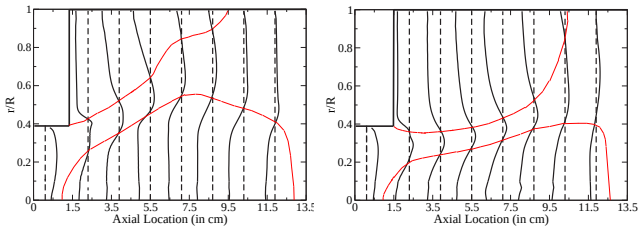

(a) $\Phi = 1.0$ (b) $\Phi = 0.45$

Figure 5. Time-averaged axial velocity profiles for $\Phi = 1.0$ and $\Phi = 0.45$. The location of the recirculation regions is also shown.

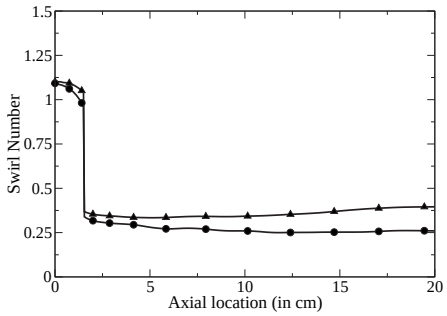

Figure 6. Time-averaged swirl number as a function of the axial location for both equivalence ratios. The dump plane is located at X = 1.5 cm (circle: $\Phi = 1.0$ - triangle: $\Phi = 0.45$

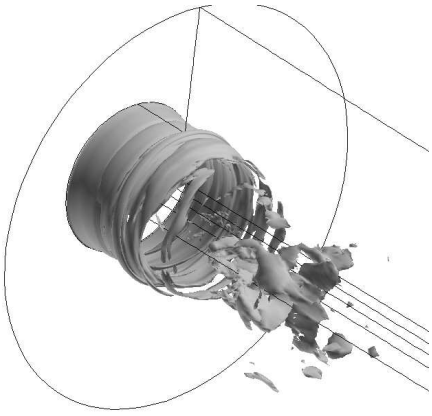

Figure 7. Instantaneous iso-surface of Ka=100. In the region where $Ka > 100$, the flame propagates in the BRZ regime.

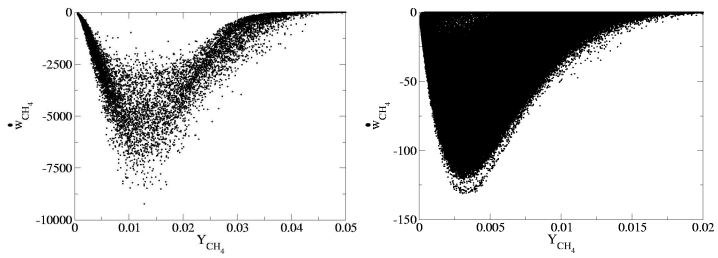

(a) $\Phi = 1.0$ (b) $\Phi = 0.45$

Figure 8. Methane reaction rate ($\widetilde{\dot{w}_{CH_4}}$) as a function of the methane mass fraction ($\widetilde{Y_{CH_4}}$).

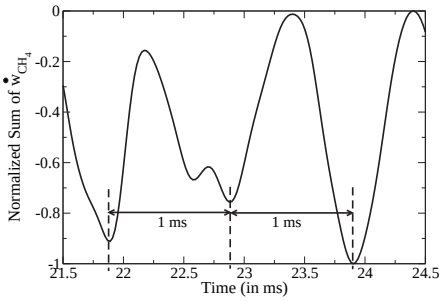

Figure 9. Normalized sum of the reaction rate in the region close to the dump plane as a function of time. The data is smoothed in order to extract the first frequency mode.

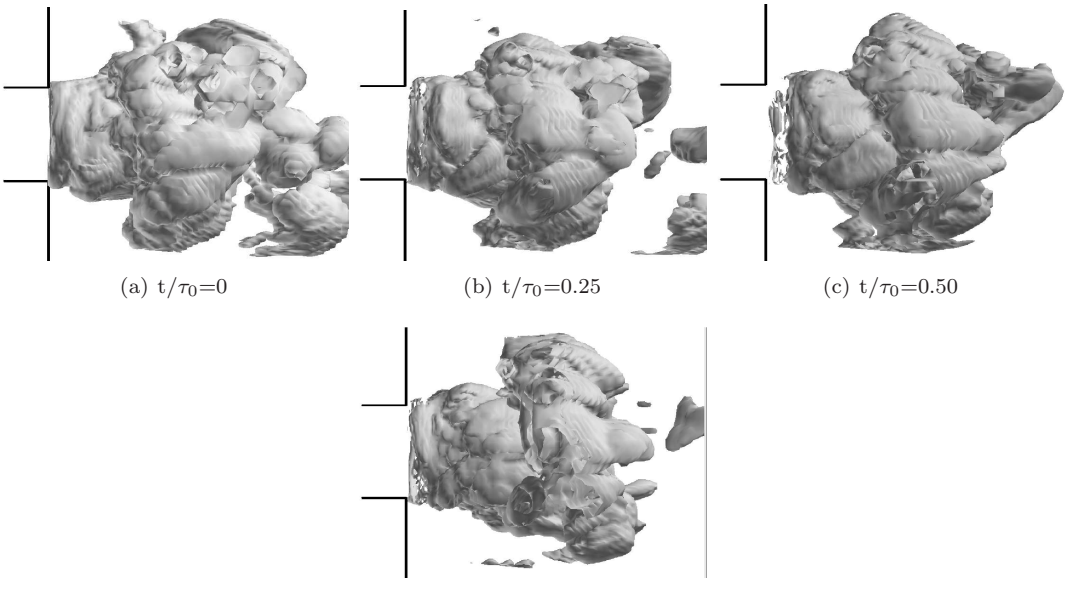

(a) t/τ_0=0 (b) t/τ_0=0.25 (c) t/τ_0=0.50

(d) t/τ_0=0.75

Figure 10. Time averaged fuel mass fraction. τ_0=1 ms.